Annual Cycle Changes in the Vertical Structure of Ocean Temperature: A Fingerprint of Human Influence on Climate

JIA-RUI SHI,[a,b] BENJAMIN D. SANTER,[a,c] YOUNG-OH KWON,[a] AND SUSAN E. WIJFFELS[a]

[a] *Woods Hole Oceanographic Institution, Woods Hole, Massachusetts*
[b] *Courant Institute of Mathematical Sciences, New York University, New York, New York*
[c] *Joint Institute for Regional Earth System Science and Engineering, University of California Los Angeles, Los Angeles, California*

(Manuscript received 28 July 2024, in final form 6 December 2024, accepted 2 January 2025)

ABSTRACT: We investigate changes in the vertical structure of the ocean temperature annual cycle amplitude ($\mathrm{TEMP_{AC}}$) down to a depth of 300 m, providing important insights into the relative contributions of anthropogenic and natural influences. Using observations and phase 6 of the Coupled Model Intercomparison Project (CMIP6) simulations, we perform a detection and attribution analysis by applying a standard pattern-based "fingerprint" method to zonal-mean $\mathrm{TEMP_{AC}}$ anomalies for three major ocean basins. In all model historical simulations and observational datasets, $\mathrm{TEMP_{AC}}$ increases significantly in the surface layer, except in the Southern Ocean, and weakens within the subsurface ocean. There is a decrease in $\mathrm{TEMP_{AC}}$ below the annual-mean mixed layer depth, mainly due to a deep-reaching winter warming signal. The temporal evolution of signal-to-noise (S/N) ratios in observations indicates an identifiable anthropogenic fingerprint in both surface and interior ocean annual temperature cycles. These findings are consistent across three different observational datasets, with variations in fingerprint detection time likely related to differences in dataset coverage, interpolation method, and accuracy. Analysis of CMIP6 single-forcing simulations reveals the dominant influence of greenhouse gases and anthropogenic aerosols on $\mathrm{TEMP_{AC}}$ changes. Our identification of an anthropogenic $\mathrm{TEMP_{AC}}$ fingerprint is robust to the selection of different analysis periods. S/N ratios derived with model data only are consistently larger than ratios calculated with observational signals, primarily due to model versus observed $\mathrm{TEMP_{AC}}$ differences in the Atlantic. Human influence on the seasonality of surface and subsurface ocean temperature may have profound consequences for fisheries, marine ecosystems, and ocean chemistry.

SIGNIFICANCE STATEMENT: The seasonal cycle is a fundamental aspect of our climate, and gaining insight into how anthropogenic forcing has impacted seasonality is of scientific, economic, and societal importance. Using observations and CMIP6 model simulations, this research applies a pattern-based detection and attribution method to ocean temperature annual cycle amplitude ($\mathrm{TEMP_{AC}}$) down to 300 m across three major ocean basins. Key findings reveal significant increases in surface layer $\mathrm{TEMP_{AC}}$ except in the Southern Ocean and a weakening of $\mathrm{TEMP_{AC}}$ within the subsurface ocean. Importantly, the analysis confirms human influence on $\mathrm{TEMP_{AC}}$. These findings underscore the profound influence of human-caused climate change on the world's oceans and have important implications for marine ecosystems, fisheries, and ocean chemistry.

KEYWORDS: Ocean; Ocean dynamics; Climate; Climate change; Pattern detection

1. Introduction

The annual cycle is one of the most fundamental elements of climate, driving over 90% of the seasonal temperature variability across much of the globe (Santer et al. 2018; Shi et al. 2024). The seasonal variation in incoming solar radiation has influence from the top of the atmosphere to the subsurface ocean. In turn, seasonal changes in temperature, moisture, and many other variables can influence human health, water supplies, agriculture, energy demand, and marine ecosystems.

The influence of human activities during the historical period has been identified in many aspects of the climate system (Eyring et al. 2021), including the substantial warming of the surface (Hegerl et al. 1996; Stott et al. 2000), the troposphere (Santer et al. 1996, 2013, 2023; Blackport et al. 2023), and the ocean (Barnett et al. 2005; Levitus et al. 2005; Wijffels et al. 2016; Shi et al. 2018; von Schuckmann et al. 2020; Cheng et al. 2019; Gleckler et al. 2016). Human fingerprints have also been identified in atmospheric and ocean circulation (Chemke and Yuval 2023; Roemmich et al. 2007; Shi et al. 2021; Swart and Fyfe 2012; Thompson and Solomon 2002; Marshall 2003) and in precipitation and atmospheric moisture (Zhang et al. 2007; Santer et al. 2007; Marvel and Bonfils 2013; Bonfils et al. 2020). The changes in these and many other variables are primarily due to anthropogenic forcing by well-mixed greenhouse gases (GHGs), ozone, and aerosols.

The scientific challenge in such climate change detection and attribution (D&A) studies is to separate human influences on climate from climate fluctuations caused by natural external forcings and internal variability. The basic premise is that different human and natural influences on climate have different characteristic spatial patterns or "fingerprints." Most of the focus in pattern-based fingerprint research has been on

---

Denotes content that is immediately available upon publication as open access.

Corresponding authors: Benjamin D. Santer, bensanter1289@gmail.com; Jia-Rui Shi, jrshi.climate@gmail.com

DOI: 10.1175/JCLI-D-24-0418.1

long-term annual-mean changes in the climate system (Gillett et al. 2013; Bindoff et al. 2013; Stott et al. 2000; Santer et al. 2019; Pierce et al. 2012; Gleckler et al. 2012). Externally forced changes in the amplitude and/or phase of the annual cycle have received less attention in formal fingerprint studies.

There is growing evidence, however, that human activities are now influencing key aspects of the annual cycle of tropospheric temperature (Santer et al. 2018, 2022), sea surface temperature (SST; Shi et al. 2024; Liu et al. 2024), land surface temperature (Qian and Zhang 2015; Duan et al. 2019), the water cycle (Marvel et al. 2017; Terray et al. 2012), and sea ice (Min et al. 2008). Previous work has shown, for example, that a human-caused signal in the annual cycle of tropospheric temperature ($\mathrm{TT_{AC}}$) is robustly identifiable in CMIP6 simulations of historical climate change and in satellite observations (Santer et al. 2018, 2022). The fingerprint of externally forced $\mathrm{TT_{AC}}$ changes had distinctive midlatitude increases in $\mathrm{TT_{AC}}$ in both hemispheres, with larger increases in the Northern Hemisphere (NH) than in the Southern Hemisphere (SH) and with $\mathrm{TT_{AC}}$ decreases in subpolar regions of the SH. The hemispheric asymmetry in $\mathrm{TT_{AC}}$ changes was related to land–ocean differences in heat capacity and hemispheric differences in land fraction (Santer et al. 2022).

An independent fingerprint analysis of changes in the SST annual cycle ($\mathrm{SST_{AC}}$) identified an externally forced pattern that was consistent with the large-scale geographical pattern of changes in the annual cycle of TT: increased $\mathrm{SST_{AC}}$ in NH midlatitudes and a distinctive meridional dipole structure at SH midlatitudes (Shi et al. 2024). In the NH midlatitudes, the $\mathrm{SST_{AC}}$ increases were primarily due to GHG-driven mixed layer depth changes associated with enhanced stratification (Alexander et al. 2018; Chen and Wang 2015; Liu et al. 2020; Jo et al. 2022; Dwyer et al. 2012; Shi et al. 2024). The reduction in thermal inertia due to the year-round shoaling of the mixed layer contributed to the enhancement of midlatitude $\mathrm{SST_{AC}}$ (Shi et al. 2024). The dipole-like $\mathrm{SST_{AC}}$ response in SH midlatitudes, however, was largely due to enhanced and poleward-shifted westerly winds over the Southern Ocean (Zhang et al. 2024).

The goal of the present study is to interrogate the annual cycle of temperature changes below the ocean surface and to determine 1) whether an anthropogenic fingerprint is identifiable in the vertical structure of $\mathrm{TEMP_{AC}}$ down to 300 m, in both state-of-the-art historical simulations and in a variety of observational products; and 2) whether analysis of the subsurface structure yields further insights into the physical drivers of $\mathrm{TEMP_{AC}}$ changes. While previous investigations have applied fingerprinting approaches to annual-mean changes in the vertical structure of ocean temperature (Barnett et al. 2005; Pierce et al. 2006, 2012) or to ocean heat content (Gleckler et al. 2012), no prior study has performed fingerprinting with $\mathrm{TEMP_{AC}}$. This previous work revealed that since 1960, an identifiable anthropogenic warming signal has penetrated the world's oceans, with the vertical structure of warming varying by basin (Barnett et al. 2005). In the North and South Atlantic Oceans, the large-scale convective overturning circulation led to deeper penetration of human-induced warming, while a warming signal was more confined to the upper layers of the northern Pacific and Indian Oceans.

Anthropogenic changes in greenhouse gases and aerosols also yield detectable changes in ocean salinity (Pierce et al. 2012; Swart et al. 2018) and in water mass properties. In the latter case, analysis of model simulations indicates that by 2020, 20%–55% of the Atlantic, Pacific, and Indian Ocean Basins have an emergent anthropogenic water mass signal (Silvy et al. 2020). All of these previous investigations of annual-mean changes in ocean temperature, salinity, and water mass properties provide robust evidence for the existence and penetration of anthropogenic signals into the subsurface ocean. Whether these annual-mean changes are accompanied by robust seasonal changes in subsurface ocean properties is the focus of our attention here. As we will show, the vertical- and basin-scale structure of $\mathrm{TEMP_{AC}}$ changes is complex, with both enhancement and weakening of $\mathrm{TEMP_{AC}}$ in specific layers and regions. Importantly, many of these vertical features in $\mathrm{TEMP_{AC}}$ are common to model simulations of historical changes and observations.

The structure of our paper is as follows. Section 2 introduces the observational data, model simulations, and methods used in this study. Section 3 discusses the vertical structure of trends based on observations and CMIP6 models. Section 4 presents the results of a signal-to-noise (S/N) analysis of the vertical structure of $\mathrm{TEMP_{AC}}$ change for three ocean basins: the Atlantic, Pacific, and Indian Oceans. Physical mechanisms driving the $\mathrm{TEMP_{AC}}$ changes are considered in section 5. Results from the analysis of single-forcing runs, providing estimates of contributions from individual external forcings, are considered in section 6. In section 7, we perform sensitivity tests to investigate how model versus observed differences in S/N behavior are affected by the choice of analysis period and the inclusion of observational information from individual ocean basins. Section 8 provides conclusions for this study.

2. Data and methods

a. *Observational datasets*

We use three gridded estimates of observed ocean potential temperature. These are datasets from the Institute of Atmospheric Physics (IAP), Met Office Hadley Centre (EN4), and the subsurface temperature analysis led by Ishii (hereafter Ishii). All three observational products are based on a variety of measurements, including shipboard conductivity–temperature–depth (CTD), mechanical bathythermograph, expendable bathythermograph (XBT), and Argo profiles. The IAP ocean potential temperature analysis has a horizontal resolution of 1° × 1° with 41 vertical levels from the surface down to 2000 m and spans the period 1940 to the present (Cheng et al. 2018). Data gaps are filled by a first-guess field incorporating time-evolving outputs from an ensemble of models taken from phase 5 of the Coupled Model Intercomparison Project (CMIP5). EN4 (version EN4.2.2) is a subsurface temperature dataset for the global oceans, spanning 1900 to the present with monthly resolution (Good et al. 2013). The XBT bias was corrected using the methods of Gouretski and Reseghetti (2010). The EN4 data are on a regular 1° × 1° grid with 42 vertical depth levels in the upper 2000 m. The subsurface temperature analysis from

Ishii has a horizontal resolution of 1° × 1° with 28 vertical levels from the surface down to 3000 m and spans the period from 1955 to the present (Ishii et al. 2005). Missing data are filled with values interpolated spatially and temporally using monthly deviations from nearby grid points.

All three observational ocean temperature datasets also provide monthly salinity. To estimate the mixed layer depth (MLD), we utilize the gridded monthly temperature and salinity data from individual datasets to calculate the potential density. MLD is then defined as the depth at which the ocean potential density exceeds the surface layer density at a criterion of $\delta\rho = 0.125\ \mathrm{kg\ m^{-3}}$, following the definition for MLD output (referred to as "mlotst") from the CMIP6 models. This facilitates the direct comparison of MLD in simulations and observations.

b. *CMIP6 model simulations*

This study uses output (ocean temperature and MLD) from climate model simulations performed under CMIP6 (Eyring et al. 2016). We focus on 10 CMIP6 models that performed all of the following four experiments: the historical all-forcing simulation (HIST) and single-forcing simulations with anthropogenic aerosols (AER), well-mixed GHGs, and purely natural changes in solar irradiance and volcanic aerosols (NAT) (Gillett et al. 2016). Each of the 10 models has multiple ensemble members. To allow a comparison of historical simulations with recent ocean observations through to 2022, we extend the HIST runs (which end in 2014) with output from one selected scenario of future climate change, shared socioeconomic pathway 2-4.5 (SSP245). Each SSP245 run was initialized from the end of a counterpart HIST run. The number of ensemble members available for each model and each experiment is listed in Table 1.

For each historical experiment, there are 51 realizations in total. Because not all HIST simulations had an SSP245 extension, there are only 42 HIST + SSP245 realizations. For simplicity, our use of the term "HIST" throughout the paper covers both the 51 HIST realizations ending in 2014 and the 42 HIST realizations extended to 2022 with SSP245 output. The multimodel mean (MMM) is the average of the ensemble means of these 10 models. The preindustrial control (piControl) simulations from the same 10 models are used for the purpose of estimating the noise from natural internal variability. Single-forcing experiments end in 2020. All model output was interpolated to a common, regular 1° × 1° horizontal grid. In the vertical direction, model fields were interpolated to depths of 5, 10, 20, 30, 50, 75, 100, 125, 150, 200, and 300 m. For each model, we then calculate zonal-mean temperature fields for the Pacific, Atlantic, and Indian Ocean Basins; the longitudes used to separate these basins in the Southern Ocean are 147°E, 69°W, and 20°E (respectively).

c. *Calculation of annual cycle amplitudes*

For each model simulation and observational product, and at each grid point x in latitude/depth/basin space and year t, we performed a Fourier analysis on the 12 monthly mean values of zonal-mean ocean temperature for each year. We define the annual cycle amplitude ($\mathrm{TEMP_{AC}}$) as the amplitude of the first harmonic. Consistent with previous work with $\mathrm{TT_{AC}}$ (Santer et al. 2018), the first harmonic explains >95% of the total seasonal variance at almost all locations between 60°N and 60°S in the upper 300 m of the ocean. There are two exceptions: 1) regions poleward of 60°N/S, which are influenced by sea ice and have limited observational coverage; and 2) the deep tropics between 15°S and 15°N, where there is little seasonal change in incoming solar radiation. In this study, we exclude both regions from our fingerprint analysis, thus focusing attention on regions which experience appreciable seasonal cycles in upper-ocean temperature and are relatively unaffected by sea ice. After the calculation of the annual cycle on the native grid of the model, $\mathrm{TEMP_{AC}}$ is interpolated vertically, which provides a uniform basis for comparing the vertical structure of modeled and observed $\mathrm{TEMP_{AC}}$ changes and for performing the fingerprinting.

Table 1. CMIP6 models and the number of model realizations used in this study. The left column shows the 10 CMIP6 models for which HIST, GHG, AER, and NAT runs were available. The middle and right columns show the number of realizations available for each model and experiment. The identifiers of these realizations (r1, etc.) are indicated in brackets.

Model names	No. of realizations used in HIST, GHG, AER, and NAT	No. of realizations used in SSP245 for 2015–22
ACCESS-CM2	3 (r1–r3)	3 (r1–r3)
ACCESS-ESM1-5	3 (r1–r3)	3 (r1–r3)
CanESM5	15 (r1–15)	10 (r1–15)
CESM2	2 (r1 and r3)	1 (r1)
CNRM-CM6-1	3 (r1–r3)	3 (r1–r3)
HadGEM3-GC31-LL	4 (r1–r4)	4 (r1–r4)
IPSL-CM6A-LR	10 (r1–r3)	7 (r1–r6, r10)
MIRO6	3 (r1–r3)	3 (r1–r3)
MRI-ESM2-0	5 (r1–r3)	5 (r1–r3)
NorESM2-LM	3 (r1–r3)	3 (r1–r3)

d. *Pattern-based fingerprint method*

To test whether a $\mathrm{TEMP_{AC}}$ response to external forcing can be identified in observations, we first need to estimate this response using the CMIP6 model simulations.

1) Definition of the fingerprint

The fingerprint $F(x)$ is the first EOF of the changes over time in the MMM $\mathrm{TEMP_{AC}}$ anomalies from the HIST experiment—i.e., the temporal changes in the annual cycle of zonal-mean temperature as a function of depth and basin. The domain is restricted to 60°S–60°N, excluding 15°S–15°N. The anomalies are weighted by the square root of the cosine of the grid node's latitude and the thickness of layers (van den Dool et al. 2000) before calculating the EOF. Our discussion focuses on model fingerprints estimated from 1980 to 2022. Due to the increased and sustained use of XBT, global upper-ocean temperature sampling stabilizes at around 75% from 1980 onward (Lyman and Johnson 2008; Meyssignac et al. 2019),

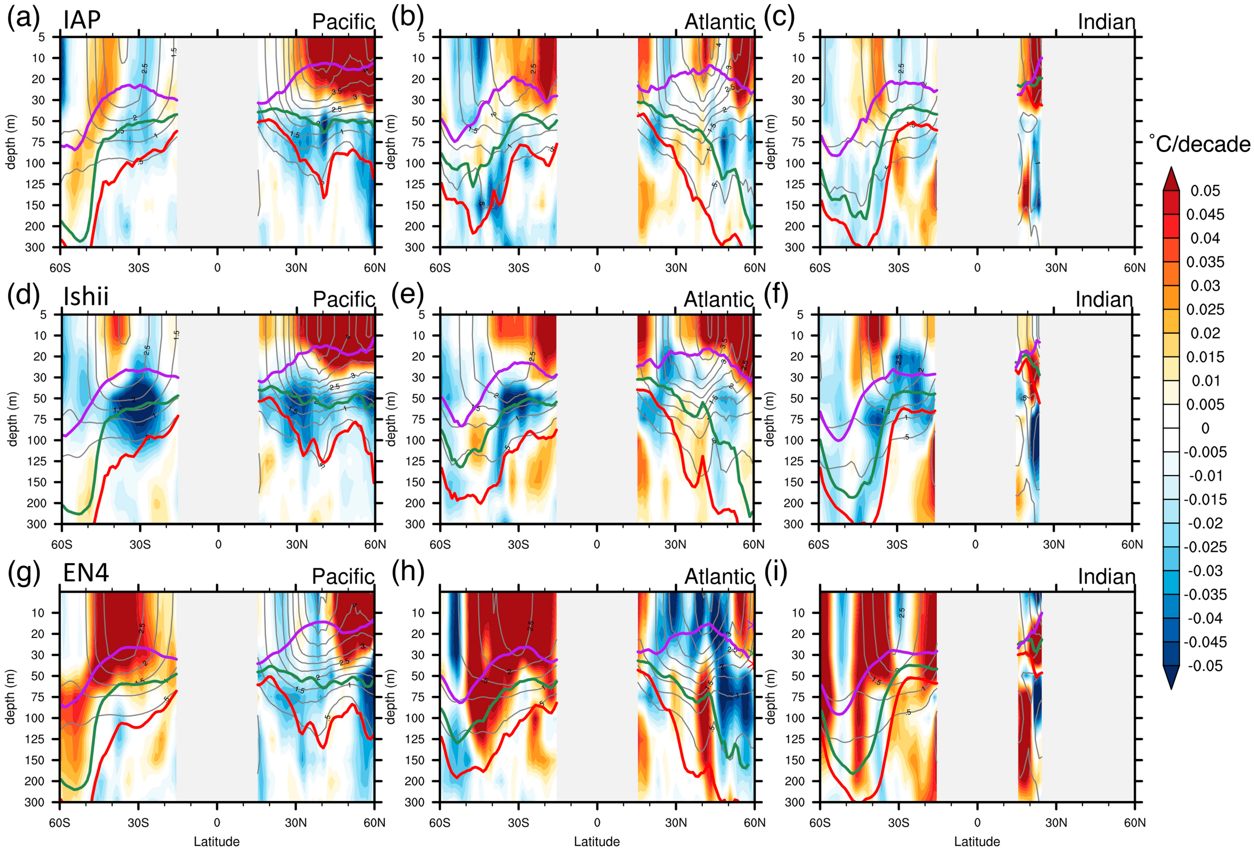

FIG. 1. Observed trends in zonal-mean TEMP$_{AC}$ over the period 1980–2022 for three different datasets and ocean basins: (a)–(c) Trends from IAP, (d)–(f) trends from Ishii, and (g)–(i) trends from EN4. Results are for the (left) Pacific, (middle) Atlantic, and (right) Indian Ocean Basins. The gray contours are climatological TEMP$_{AC}$ values over 1980–2022 for the corresponding basin and dataset. Purple, green, and red curves show the summertime (July–September mean for the NH or January–March mean for the SH), annual mean, and wintertime MLD, respectively, averaged over the analysis period.

thus providing adequate coverage for estimating large-scale observed ocean temperature changes.

2) FINGERPRINT DETECTION

Our detection method assesses whether the similarity between observed TEMP$_{AC}$ patterns and $F(x)$ shows a statistically significant trend over time. The observed TEMP$_{AC}$ anomalies are projected onto $F(x)$ to derive a signal time series $Z_o(t)$. We assess the statistical significance of trends in $Z_o(t)$ by comparing them to a null distribution derived from noise time series $N_c(t)$. Noise here is estimated using the 4000-yr concatenated noise dataset from the piControl runs of 10 models (using the last 400 years from each model). Signal detection occurs when the trend in $Z_o(t)$ exceeds the 5% significance level and then remains continuously above this level for all longer analysis periods. Model-only results are also computed, replacing observational estimates of TEMP$_{AC}$ changes with changes from HIST simulations. The baseline analysis uses a minimum trend length of 10 years. Our primary focus is on the period 1980–2022. Additionally, we test the sensitivity of our fingerprint results to the use of different analysis periods (see section 7a). More details on the fingerprinting approach can be found in Shi et al. (2024).

3. Trends and forced responses of TEMP$_{AC}$

Observed patterns of TEMP$_{AC}$ trends during the analysis period (1980–2022) exhibit a common vertical structure in most ocean basins (Fig. 1). Above the summertime (or annual mean) MLD in each hemisphere, TEMP$_{AC}$ trends are predominantly positive in most ocean regions, except in the Southern Ocean (particularly south of 50°S), where they are negative (albeit weaker). This large-scale upper-ocean trend pattern is consistent with the results from an independent analysis of changes in the annual cycle of SST (SST$_{AC}$; Shi et al. 2024). Climatologically, TEMP$_{AC}$ is largest in the midlatitudes in both hemispheres and above the wintertime MLD, decreasing markedly in amplitude below the wintertime MLD.

In addition to the near-surface increases noted above, TEMP$_{AC}$ decreases in certain subsurface regions, such as at 50–100-m depth in the South Atlantic and South Pacific and at midlatitudes in the North Pacific. Negative trends penetrate deeper in the higher latitudes in the North Atlantic and North

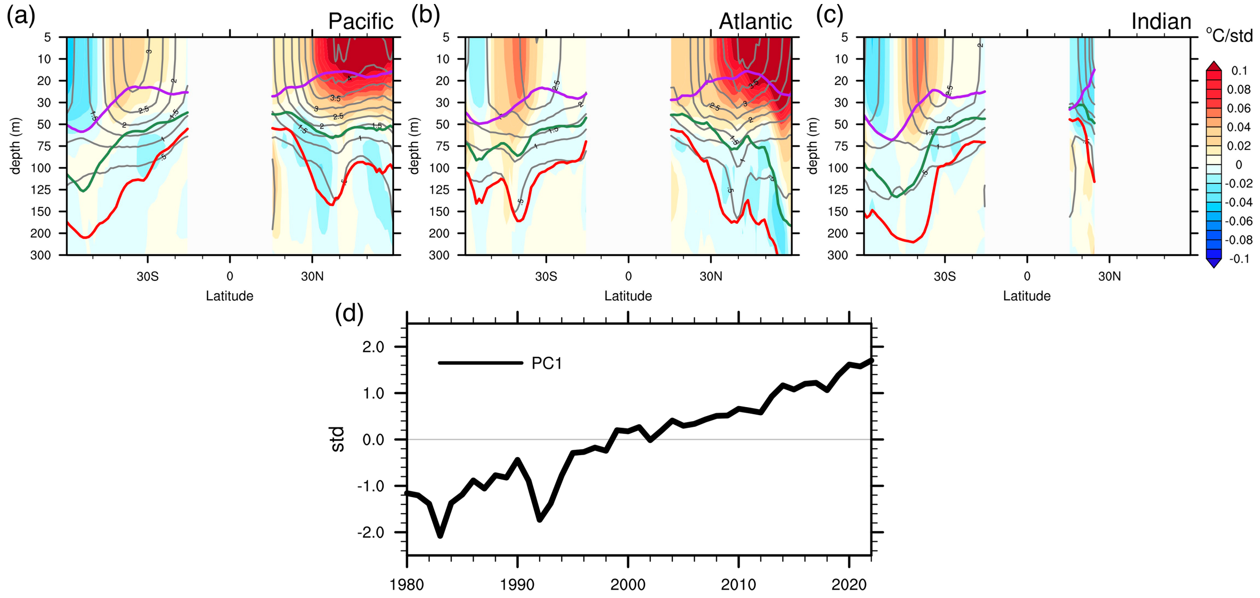

FIG. 2. The HIST MMM fingerprint pattern of $\mathrm{TEMP}_{\mathrm{AC}}$, which is defined here as the EOF1 of the MMM $\mathrm{TEMP}_{\mathrm{AC}}$ change over the period 1980–2022. (a)–(c) The results for the three basins shown here are the regression patterns on the (d) standardized first principal component. The variance explained by this first mode is approximately 51%.

Pacific. These reductions in $\mathrm{TEMP}_{\mathrm{AC}}$ primarily occur between the summertime MLD (purple curve in Fig. 1) and wintertime MLD (red curve in Fig. 1)—that is, within the lower part of the seasonal thermocline.

There are also some notable differences across the three observed datasets. The results from the IAP and Ishii datasets are generally consistent in terms of their spatial patterns and trend magnitudes, with an uncentered pattern correlation of $R = 0.74$ for the three concatenated basin zonal averages (i.e., when the patterns for the three basins are considered jointly rather than individually). In all three basins, however, the Ishii data have larger negative $\mathrm{TEMP}_{\mathrm{AC}}$ trends in the SH relative to the IAP data (Figs. 1a–f). Compared with the other two datasets, the EN4 dataset shows larger long-term trends in the surface layer and is noticeably different from the other two datasets in the North Atlantic above the summertime MLD (Figs. 1g–i). In the North Pacific and North Atlantic, the EN4 dataset has weak negative trends in the midlatitudes, where the mean annual cycle is strongest (see contours in Fig. 1). The uncentered pattern correlations between $\mathrm{TEMP}_{\mathrm{AC}}$ trends in EN4 and IAP and between $\mathrm{TEMP}_{\mathrm{AC}}$ trends in EN4 and Ishii are $R = 0.53$ and $R = 0.36$, respectively. These differences across datasets reflect the structural uncertainty arising from differences in the choices of raw data analyzed, bias correction procedures, and gap-infilling methods. The differences across datasets are also sensitive to the choice of analysis period (see section 7). All three datasets, however, show generally positive $\mathrm{TEMP}_{\mathrm{AC}}$ changes in the surface layer and negative $\mathrm{TEMP}_{\mathrm{AC}}$ changes in the subsurface ocean.

We obtain an estimate of the simulated $\mathrm{TEMP}_{\mathrm{AC}}$ response to combined anthropogenic and natural external forcing by EOF analysis of the HIST MMM $\mathrm{TEMP}_{\mathrm{AC}}$ changes over 1980–2022. This estimate is the fingerprint $F(x)$—the first EOF mode (see section 2d). The fingerprint displays a number of large-scale features evident in the observed $\mathrm{TEMP}_{\mathrm{AC}}$ trends in Fig. 1. Examples of such common features include increases in zonal-mean $\mathrm{TEMP}_{\mathrm{AC}}$ in the surface layers and decreases south of ~50°S and below the annual mean MLD (Figs. 2a–c). Consistent with previous findings involving tropospheric temperature and SST, $F(x)$ exhibits considerable hemispheric asymmetry in the amplitude of $\mathrm{TEMP}_{\mathrm{AC}}$ changes, with larger midlatitude increases in upper-ocean $\mathrm{TEMP}_{\mathrm{AC}}$ in the North Pacific and North Atlantic than in the South Pacific and South Atlantic (Santer et al. 2018, 2022; Shi et al. 2024). Calculation of $F(x)$ using only two realizations from each model yields very similar patterns to those shown in Fig. 2, pointing toward the robustness of the forced response. In observations, a similar hemispheric asymmetry in $\mathrm{TEMP}_{\mathrm{AC}}$ change is found clearly only in the Pacific Ocean Basin in the IAP and Ishii datasets (Figs. 1a,d).

The time evolution of the first principal component of the HIST MMM annual cycle changes shows a steady increase during the analysis period 1980–2022 (see Fig. 2d). There are two major decreases before the year 2000, which are linked to perturbations to the annual cycle arising from the cooling effects of the El Chichón and Pinatubo volcanic eruptions. The large initial signatures of these two eruptions on $\mathrm{TEMP}_{\mathrm{AC}}$ are clearly apparent in the NAT experiment (not shown). Annual cycle amplitude recovers to pre-eruption levels within 3–4 years.

In the following section, we consider some of the basic S/N properties of $\mathrm{TEMP}_{\mathrm{AC}}$ before evaluating whether a model-predicted fingerprint of forced changes in $\mathrm{TEMP}_{\mathrm{AC}}$ is statistically identifiable in observations and individual model HIST realizations.

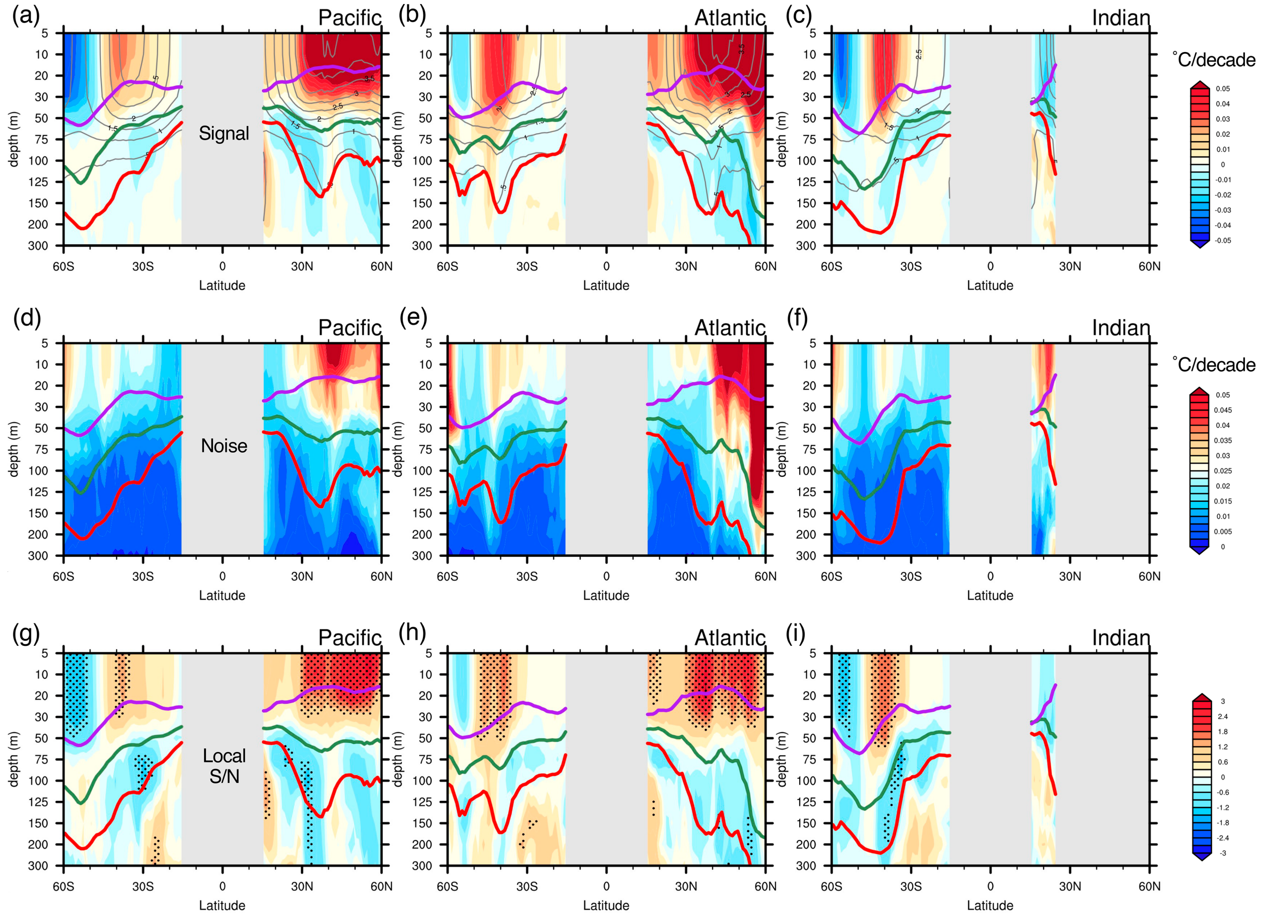

FIG. 3. Local signals, noise, and S/N ratios in CMIP6 HIST realizations. (a)–(c) Signal: trends of zonal-mean $\mathrm{TEMP_{AC}}$ over the period 1980–2022 in the MMM. As in Fig. 1, purple, green, and red curves show the climatological summertime, annual mean, and wintertime MLD. (d)–(f) Noise: standard deviation of the 42 individual $\mathrm{TEMP_{AC}}$ trends, which are weighted to account for model differences in the number of realizations. (g)–(i) Ratio between signal and noise. Stippling in (g)–(i) denotes grid points where $|S/N| > 1$.

4. Results of local S/N and fingerprint analysis

a. Local S/N analysis

Before conducting the pattern-based S/N analysis, we first calculate the S/N ratios at individual grid points in the zonal-mean $\mathrm{TEMP_{AC}}$ fields of the three ocean basins. Following the definition from previous studies (Deser et al. 2014; Santer et al. 2019), local S/N is the ratio between the trend of the ensemble-mean field at an individual location (in this case, the latitude band at a particular depth and for a given ocean basin) and the standard deviation of the trend across realizations and models at the same location. In contrast to the analysis of single-model large initial condition ensembles (Santer et al. 2019), the between-realization standard deviation of the trend estimated here does not reflect internal variability alone—it is also affected by signal and noise differences across the 10 models in the MMM (Hawkins and Sutton 2009; Lehner et al. 2020).

The vertical and latitudinal structure of the local signal (Figs. 3a–c) is broadly consistent with the fingerprint patterns inferred from the EOF analysis (Figs. 2a–c). The local noise is largest in the surface layer and decreases markedly below the annual-mean MLD (Figs. 3d–f). Dividing the signal trends in row 1 of Fig. 3 by the between-realization noise trends in row 2 yields the S/N ratios in Figs. 3g–i. The largest local S/N ratios are located in the NH mid- to high latitudes, which is consistent with findings from previous studies for $\mathrm{TT_{AC}}$ (Santer et al. 2018, 2022). The meridional dipole structure of trends between 30° and 60°S is apparent in all three ocean basins, with $|S/N| > 1$. Smaller areas with significant local S/N ratios also occur below 50 m. Although the $\mathrm{TEMP_{AC}}$ changes in the ocean interior are smaller than those in the surface layer, the following section shows that the interior ocean also contributes to the detection of the model-predicted latitude–depth fingerprint in observation-based data and individual HIST realizations.

b. Pattern-based S/N analysis

As described above (see section 2d), we use a standard pattern-based method to determine whether the model-simulated externally forced fingerprint of $\mathrm{TEMP_{AC}}$ changes is statistically

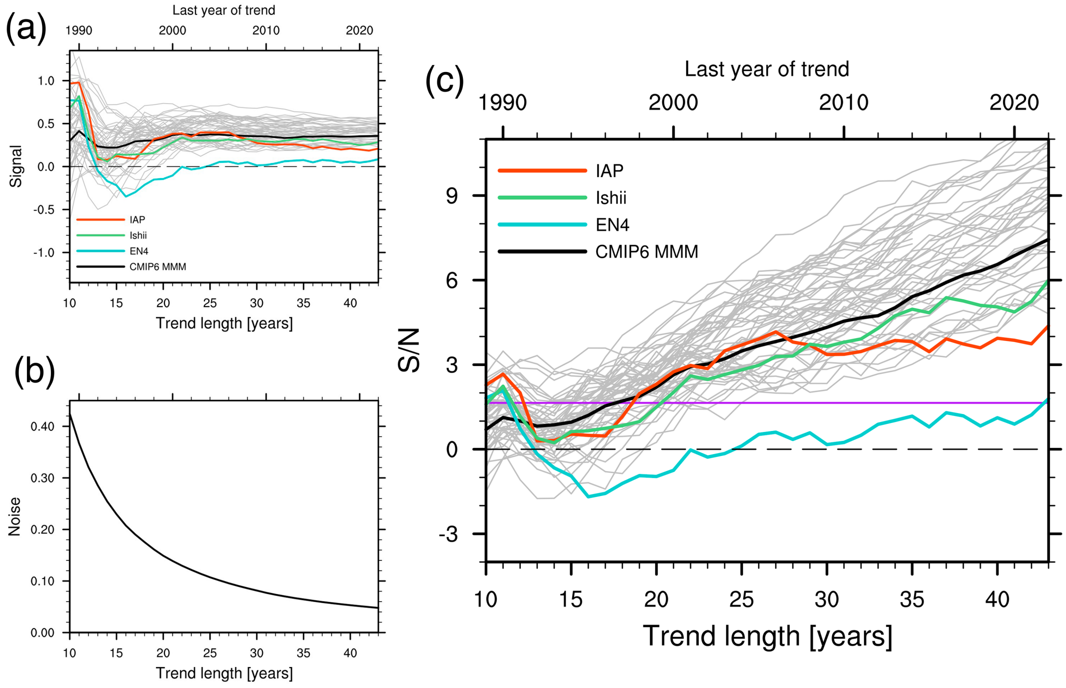

Fig. 4. Signal, noise, and S/N ratios in models and observed TEMP$_{AC}$ obtained with a standard pattern-based fingerprint method. (a) The signals are calculated by projecting TEMP$_{AC}$ from different datasets and HIST realizations onto the fingerprint estimated from the HIST MMM and then by fitting linear trends of increasing length L years to the resulting time series. (b) The noise is estimated by projecting CMIP6 control run TEMP$_{AC}$ data onto the same fingerprint, fitting nonoverlapping L-year trends to the resulting projection time series, and then calculating the standard deviation of the L-year trend distribution. (c) Time scale–dependent S/N ratios for trends calculated from signal and noise time series for the period 1980–2022. The HIST MMM result is the black curve; results from individual HIST runs are the gray curves. The colored lines denote S/N ratios estimated by searching for the HIST MMM TEMP$_{AC}$ fingerprint in three different observational datasets. The horizontal purple line is the 5% significance level.

identifiable in historical observations (Hasselmann 1979; Santer et al. 2013). Recall that the fingerprint is obtained from the multimodel average TEMP$_{AC}$ changes in the HIST simulations (Figs. 2a–c). The signal in Fig. 4a is a measure of the similarity between the fingerprint and the time-varying spatial features of ocean temperature change in observations or in individual HIST simulations. Similarly, the noise in Fig. 4b contains information on the correspondence between the fingerprint and time-varying spatial features of internal variability in model control runs. The values of S, N, and the S/N ratio (Fig. 4c) are given for a range of time scales L (in years), where L is the length of the analysis period used to calculate the least squares linear trends since the start year (1980 here).

We first consider the behavior of the signal. As expected, the model spread in signal trends (the gray lines in Fig. 4a) decreases with increasing length of the analysis period. This decrease in signal spread arises because the amplitude of the noise superimposed on the signal is markedly reduced with larger L (Fig. 4b). With longer analysis periods, therefore, there is less random similarity between the searched-for fingerprint and intrinsic variability patterns (Santer et al. 2018, 2022; Shi et al. 2024). Note that in all model- and observation-based results in Fig. 4a, signal trends decrease markedly for L-year trends ending after 1991, recovering gradually over the following decade, and then remain positive for L greater than 20–25 years. This pronounced decrease in signal strength is associated with the effects of the Pinatubo eruption in June 1991. As our results indicate, there is both model and observational evidence that Pinatubo perturbed the annual cycle of zonal-mean ocean temperature in the uppermost 300 m of the Pacific, Atlantic, and Indian Oceans.

Consistent with the discrepancies found in the observational trend patterns in Fig. 1, the EN4 dataset has signal behavior very different from that of IAP, Ishii, and the model simulations (Fig. 4a). For L greater than roughly 18 years, signals estimated with EN4 data are always smaller than in IAP, Ishii, and all model HIST realizations. After Pinatubo, the signal strength inferred from EN4 requires decades to return to positive values—far longer in any other case. Our results imply that the signal behavior in EN4 is well outside the range of what could be plausibly expected due to internal variability or large intermodel differences. The EN4 signal results are more consistent with those in IAP, Ishii, and the HIST runs after the 1990s (see section 7).

A key result from Fig. 4c is that the model zonal-mean fingerprint of TEMP$_{AC}$ changes is identifiable with high statistical confidence (i.e., at the 5% significance level or better) in all three observational datasets. In the case of the EN4 dataset,

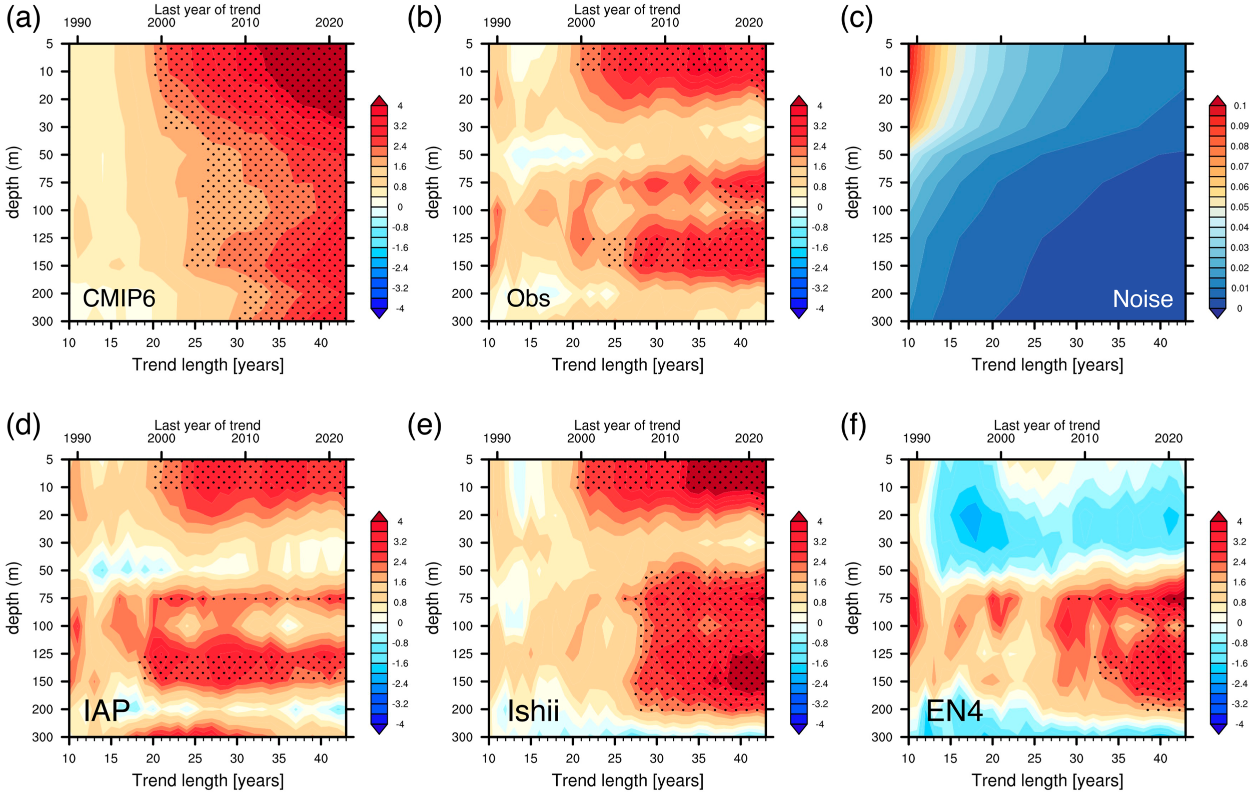

FIG. 5. "Individual layer" fingerprint analysis of $\mathrm{TEMP}_{\mathrm{AC}}$ changes for three basins (Atlantic, Pacific, and Indian Oceans). (a) Time scale–dependent S/N ratios for individual depth levels based on the fingerprint from HIST MMM for the period 1980–2022. The analysis is conducted for 11 individual layers, from the surface to 300-m depth. Stippling denotes layers and time scales for which the S/N analysis yields continuous exceedance of the 5% significance threshold. (b) S/N ratios based on the average of the three observation-based datasets: IAP, Ishii, and EN4. (c) The standard deviations of distributions of L-year trends in noise time series, inferred from the projection of the control run $\mathrm{TEMP}_{\mathrm{AC}}$ data onto the individual layer fingerprints. (d)–(f) S/N ratios based on IAP, Ishii, and EN4, respectively. The three ocean basins are analyzed jointly rather than individually in all analyses shown in this figure.

however, S/N only surpasses the critical 5% threshold for the longest analyzed period (i.e., for 43-yr trends ending in the year 2022). The $\mathrm{TEMP}_{\mathrm{AC}}$ fingerprint is also identifiable at the 5% level in all 51 individual HIST realizations (gray curves in Fig. 4c). The detection year in the model realizations invariably occurs before 2004. This result is consistent with the detection time of $\mathrm{SST}_{\mathrm{AC}}$ change found in Shi et al. (2024). Our results highlight the robustness of the externally forced $\mathrm{TEMP}_{\mathrm{AC}}$ signal to model differences in the imposed anthropogenic and natural forcing, in the response to forcing, and in the amplitude and patterns of intrinsic variability.

The fingerprint for $\mathrm{TEMP}_{\mathrm{AC}}$ changes is a complex function of depth and basin, often displaying a reversal in the sign of change between the summertime mixed layer and the portion of the water column extending from the bottom of the mixed layer to 300 m (Fig. 2). To isolate the contributions of different layers to the overall S/N results in Fig. 4, we examined the S/N properties of each of the 11 individual layers comprising the surface to 300-m latitude–depth fingerprint (Fig. 5). In the HIST MMM, the $\mathrm{TEMP}_{\mathrm{AC}}$ changes yield positive S/N ratios in each layer and for each value of L, with S/N increasing as the analysis period lengthens (Fig. 5a). The largest simulated S/N values are in the uppermost 30 m, with a subsidiary S/N maximum at ca. 150 m. Consistent with the largest local S/N values in the upper 30 m of the Pacific, Atlantic, and Indian Oceans (Fig. 3), the earliest detection of the "individual level" $\mathrm{TEMP}_{\mathrm{AC}}$ fingerprint from the MMM field is in the layers above 30 m (Fig. 5a). As depth increases below 30 m, fingerprint detection occurs later in time. The change in detection time with increasing depth is not monotonic. In the individual-level analysis, fingerprint detection in the MMM invariably occurs before 2010.

The S/N patterns in Fig. 5a show significant values in all analyzed layers. The layer above 30 m has the largest S/N. The "individual level" S/N analysis suggests that both the enhancement and weakening of $\mathrm{TEMP}_{\mathrm{AC}}$ are statistically significant—both the surface–30- and 30–300-m layers of the ocean contribute to our robust detection of the "all depths" fingerprint in different observational datasets and in each HIST realization (see Fig. 4c).

Projecting the observational-average $\mathrm{TEMP}_{\mathrm{AC}}$ changes (averaged over the IAP, Ishii, and EN4 datasets) onto the MMM "individual layer" fingerprints yields S/N results that are qualitatively consistent with the model S/N (Fig. 5b). The S/N ratio for the observational average is characterized by distinct layers of high values: an "upper layer" (0–30 m) and an "interior layer" (75–300 m). As expected, the observation-based S/N ratio is considerably lower than in the model results because the observations have only one manifestation of internal variability—i.e., internal variability is not being damped by averaging over realizations and models.

In both the simulations and observations, the complex structure of S/N as a function of depth reflects changes in the relative strengths of signal and noise. The individual layer fingerprinting (Fig. 5c) and the local S/N analysis (Figs. 3d–f) both reveal that the amplitude of the noise decreases abruptly below around 50 m. This is favorable for the detection of forced signals penetrating deeper into the ocean during winter (see section 5).

We also searched for the same model-predicted individual layer fingerprints in the three observational datasets (Figs. 5d–f). The S/N ratios obtained with the IAP and Ishii datasets are similar. A small difference is in the detection year in the interior layer: the IAP dataset yields a similar detection year in the upper layer and interior layer, while detection is delayed by ca. 5 years in the interior layer in the Ishii dataset (Figs. 5d,e). Many of the XBT, MBT, Bottle data sources used in our three observational products have positive biases. IAP implemented bias corrections for some of these issues, which likely contributes to the IAP versus Ishii S/N differences in Figs. 5d and 5e. As in the all-depth fingerprint analysis, the EN4 dataset shows S/N behavior distinctly different from that in IAP, Ishii, and the model simulations (Fig. 5f). The S/N ratios for EN4 have opposite signs in the upper layer and interior ocean and only show significant, positive values in the interior. Comparing the all-depth fingerprint with the trend pattern from the EN4 dataset (cf. Figs. 1g–i and 2a–c) reveals that the discrepancy between EN4 and other datasets arises mainly from the midlatitude Pacific and Atlantic in the surface layer. These mismatches between the patterns of $\mathrm{TEMP_{AC}}$ change in EN4 and in the model fingerprint contribute to the small and nonsignificant S/N ratios obtained in the surface layer for EN4 (Fig. 5f).

5. Physical mechanisms

We seek to understand the physical mechanisms that drive the $\mathrm{TEMP_{AC}}$ changes described above. The midlatitude amplification of $\mathrm{SST_{AC}}$ is linked to changes in MLD in the NH (Dwyer et al. 2012; Alexander et al. 2018; Jo et al. 2022; Shi et al. 2024) and to changes in wind stress in the SH. The change in the annual cycle of upper-ocean temperature found here is consistent with the $\mathrm{SST_{AC}}$ results. Our focus, therefore, is on the subsurface, particularly on possible physical mechanisms related to the weakening of the annual cycle within the seasonal thermocline.

Relevant process information is available in the changes in NH monthly mean temperature in CMIP6 models and two datasets (IAP and Ishii; see Fig. 6). The long-term warming trend for summertime is markedly larger than that of the wintertime in the surface layer, resulting in the enhancement of the annual cycle (Figs. 6a,d,g). In contrast, for the interior layer, the increase in temperature during wintertime is larger than during summertime. This winter warming is mixed down to the deeper winter mixed layer. The consistency of these seasonal temperature changes in models and observations suggests that the weakening of $\mathrm{TEMP_{AC}}$ in the interior layer is associated with the penetration to depth of surface warming associated with the deep wintertime mixed layer.

A comparison of the vertical profiles of winter and summer temperature supports this mechanism (Figs. 6b,e,h). During summer, the ocean warming below the strong vertical gradient of temperature (i.e., seasonal thermocline) is weaker, as warming is confined to the shallow summer mixed layer (dashed curves in Figs. 6c,f,i). During winter, however, the warming penetrates much deeper with a relatively uniform vertical distribution within the winter mixed layer. The wintertime warming in models and observations is therefore larger than the more surface-trapped summertime warming in the depth range corresponding to the seasonal thermocline (Figs. 6c,f,i). This winter–summer warming difference in the interior layer is smaller in the HIST runs than in observations, because the simulated warming at this level is larger than observed during summer, which in turn is likely related to too strong diffusion of upper-layer warming into the interior ocean, and varying MLDs among the simulations and models. Multidecadal internal variability in observations—which is damped by averaging over realizations and models in the HIST MMM—must also contribute to the winter–summer warming difference between models and observations (Po-Chedley et al. 2021, 2022).

6. Contributions from individual external forcings

We use CMIP6 single-forcing simulations to isolate and quantify the individual contributions of well-mixed GHGs, AER, and volcanic eruptions and solar variability (NAT) to the above-described $\mathrm{TEMP_{AC}}$ changes in the HIST simulations. Consistent with the approach in Shi et al. (2024), contributions of individual external forcings to the time-evolving $\mathrm{TEMP_{AC}}$ changes obtained with the GHG, AER, and NAT single-forcing simulations are all regressed onto the same HIST fingerprint pattern (Figs. 2a–c).

In 84% and 73% of the GHG and AER simulations (respectively), the S/N exceeds the 5% threshold by the end of the single-forcing run in 2020 (Figs. 7a,b). The S/N ratios for the GHG and AER cases increase nearly linearly with increases in time scale L. In contrast, the S/N results for $\mathrm{SST_{AC}}$ change due to AER forcing showed markedly nonlinear behavior over the longer analysis period of 1950–2014 in Shi et al. (2024). The nonlinearity in $\mathrm{SST_{AC}}$ is related to nonlinear changes in emissions of $\mathrm{SO_2}$, with increasing emissions from the late 1950s to the 1970s followed by a reduction in $\mathrm{SO_2}$ emissions from North America and Europe after the 1980s (Deser et al. 2020; Bonfils et al. 2020; Shi et al. 2022, 2023). The linear behavior of $\mathrm{TEMP_{AC}}$ seen here is consistent with the more linear change in $\mathrm{SO_2}$ emissions over our shorter 1980–2022 analysis period (Fig. 7b). The AER forcing augments the GHG signal due to the above-noted post-1980 reduction of aerosol emission in the North America and Europe (Shi et al. 2022, 2023).

The contribution from AER forcing to the total S/N ratios found here is appreciable. For example, the S/N ratio from

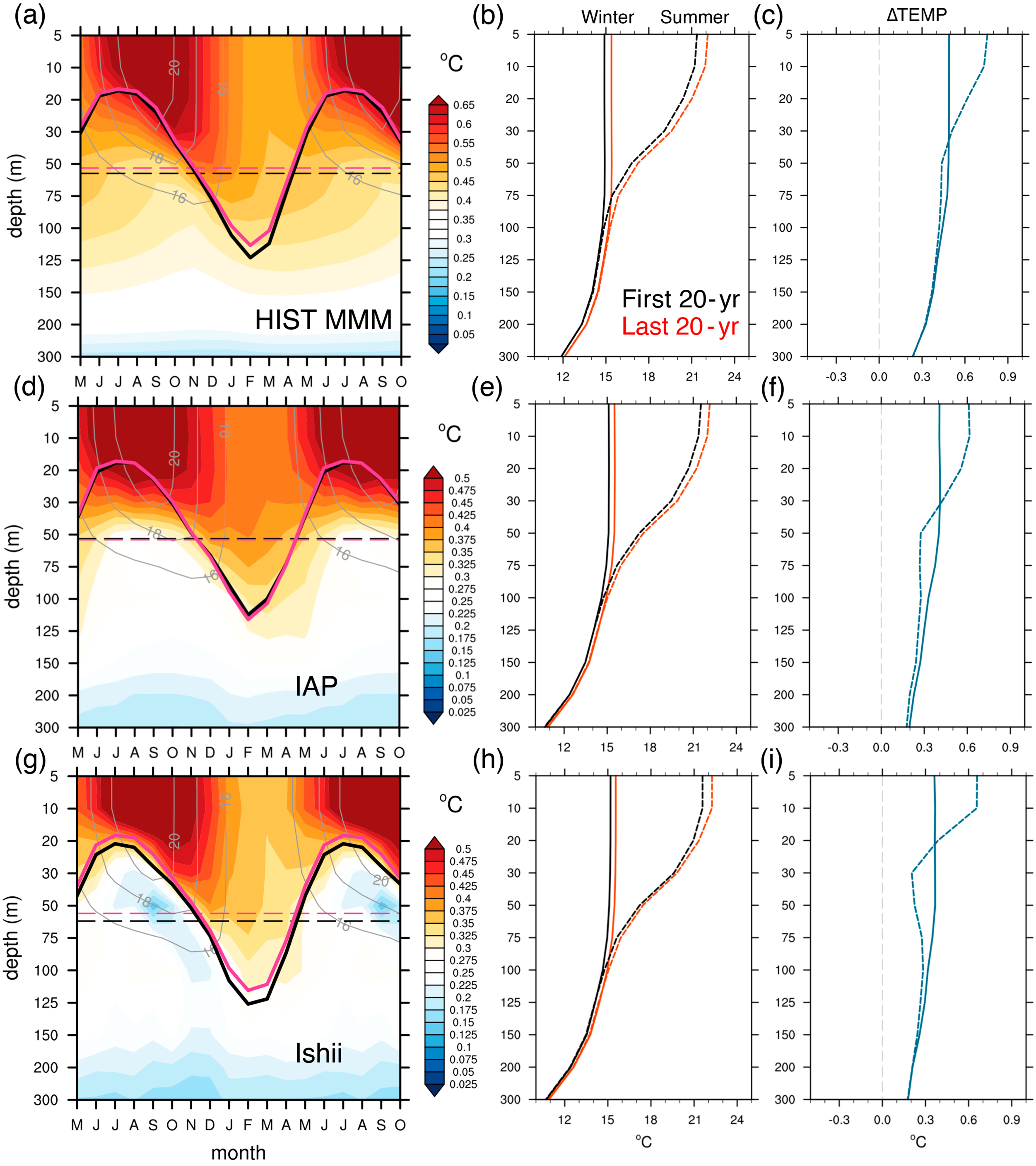

FIG. 6. Monthly mean ocean temperature changes averaged over 15°–60°N. Results are the difference between the first 20 years of our primary 43-yr analysis period (1980–99 average) and the last 20 years (2003–22 average). (a),(d),(g) Monthly differences estimated from HIST MMM, IAP, and Ishii. The gray contours denote the climatology of ocean temperature over the full 43-yr analysis period. Black and red curves are MLD from the first 20 years and the last 20 years, respectively. The dashed horizontal lines show the annual mean MLD in the two 20-yr periods. (b),(e),(h) The vertical profile of winter (solid curve) and summer (dashed) temperature from HIST MMM, IAP, and Ishii. Black and red curves are mean temperature from the first 20 years and the last 20 years, respectively. (c),(f),(i) TEMP changes between the first 20 years and the last 20 years for winter (solid curve) and summer (dashed curve).

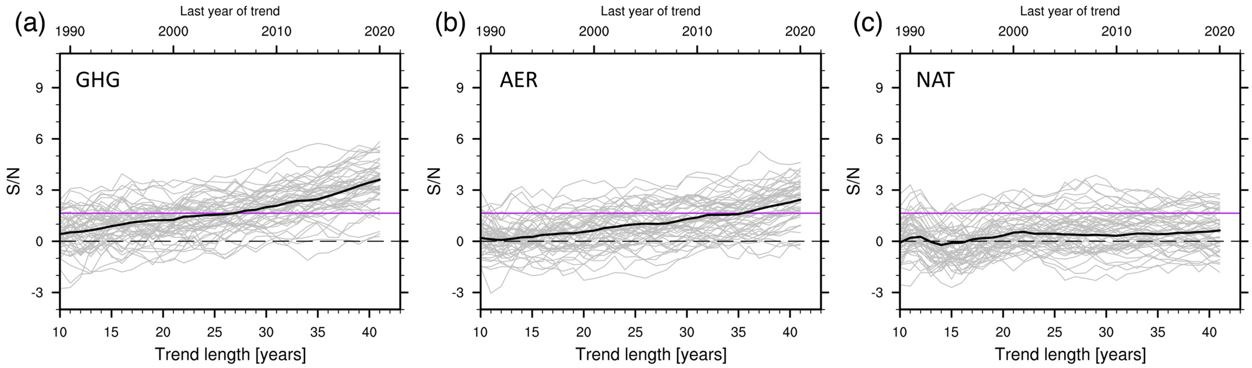

FIG. 7. S/N ratios from CMIP6 single-forcing runs: (a) GHG, (b) AER, and (c) NAT. S/N ratios were obtained by a fingerprint analysis involving the pattern of $\mathrm{TEMP_{AC}}$ change estimated from the HIST MMM (see Fig. 2). The result from the MMM of each single-forcing experiment is shown as the black curve; results from individual realizations are the gray curves. The horizontal purple line is the 5% significance level.

the AER MMM reaches 2.43 by the end of 2020, compared with 3.63 for the GHG MMM. Relative to the S/N result from HIST (6.85), GHG and AER forcings contribute 53% and 35%, respectively. It is worth noting here that in our previous work with $\mathrm{SST_{AC}}$, linear additivity was a reasonable assumption—i.e., the sum of the S/N contributions from individual forcings was very similar to the S/N result obtained in the HIST "all forcings" case (Shi et al. 2024). The detection year in the MMM is five years earlier for GHG (ca. 2005) than for AER (ca. 2010).

For the NAT single-forcing integration, only 27% of the S/N ratios for the individual realizations yield statistically significant results (Fig. 7c). This implies that any long-term (multidecadal) effect of volcanic and solar forcing on $\mathrm{TEMP_{AC}}$ change is relatively small and is probably due to the timing of two large volcanic eruptions (El Chichón and Pinatubo) relative to the length of the analysis period. The previously mentioned effect of Pinatubo on signal trends and S/N ratios (see Figs. 4a,c) is also evident in NAT.

7. Sensitivity tests

a. *Sensitivity to the analysis period*

The first sensitivity test we performed was to explore the impact of the choice of analysis period on the fingerprint results. The observational datasets examined here provide estimates of ocean temperature from 1940 onward for IAP data and even from as early as 1900 for EN4 data. These early observations are highly uncertain due to poor spatial coverage, particularly at depth (Good et al. 2013). Our primary analysis period, 1980–2022, has adequate continuous coverage for estimating large-scale ocean temperature changes. In the following, we also show the S/N results for a longer analysis period (1960–2022) and for a shorter period (1990–2022).

The spatial structure of the fingerprint patterns estimated for the 1960–2022 and 1990–2022 periods (not shown) does not change markedly relative to the fingerprint shown in Figs. 2a–c for 1980–2022. This is consistent with the temporal stability of the $\mathrm{TT_{AC}}$ fingerprint pattern in previous studies (Santer et al. 2018, 2022). For 1960–2022, the fingerprint of long-term changes in $\mathrm{TEMP_{AC}}$ is identifiable in all HIST realizations and in all three observational datasets (Fig. 8a). As in the case of our baseline 1980–2022 analysis period, S/N ratios calculated by projecting IAP and Ishii $\mathrm{TEMP_{AC}}$ data onto the searched-for fingerprint are near the lower end of the model results for the longest trends. EN4 remains an outlier, with an S/N ratio for the longest (63-yr) analysis period that is markedly lower than in IAP, Ishii, or any of the model realizations, and with substantially different time evolution of S/N.

Note that S/N results for 1960–2022 are larger than those for 1980–2022 (cf. Figs. 4c and 8a). This is primarily due to the reduction in noise amplitude with increasing length of the analysis period (see Fig. 4b). Detection times for 1960–2022 are close to the year 2000, except in the case of EN4, and are consistent with the detection times estimated with the shorter 1980–2022 analysis period. Similar detection time results are obtained for 1990–2022 (Fig. 8b). As for the two longer periods, fingerprint detection occurs in every model HIST realization and observational dataset. For S/N ratios calculated over the full 1990–2022 period, results obtained with the Ishii dataset are close to the center of the spread of model results, and EN4 results are now close to those of IAP and less of an outlier than for longer analysis periods.

b. *Sensitivity tests with annual cycle changes in individual ocean basins*

It is of interest to determine how our overall fingerprint results for global-scale changes in $\mathrm{TEMP_{AC}}$ are influenced by the annual cycle behavior in individual ocean basins. As shown in Figs. 4c and 8, the S/N ratios for the longest analysis periods are generally smaller in observational data than in the HIST MMM and are close to the lower end of the spread obtained from individual model HIST realizations. The possible causes of such differences include the effects of climate sensitivity and multidecadal internal variability and (Po-Chedley et al. 2021, 2022; Santer et al. 2022; Shi et al. 2024). Our test here examines the separate contributions to these systematic differences arising from $\mathrm{TEMP_{AC}}$ changes in the Atlantic and Pacific.

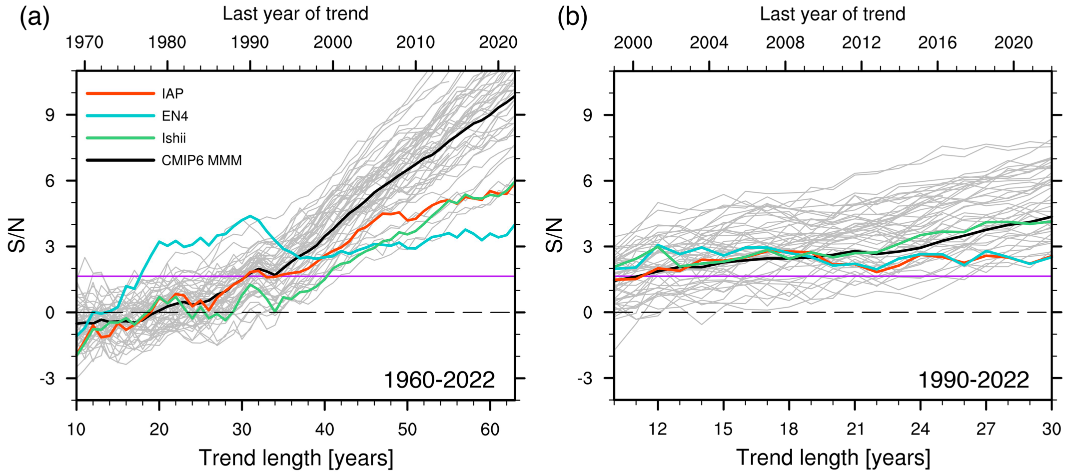

FIG. 8. As in Fig. 4c, but for analysis periods of (a) 1960–2022 and (b) 1990–2022. The fingerprints are calculated over 1960–2022 and over 1990–2022, respectively.

To isolate these contributions, we repeated the "three basin" fingerprint analysis shown in Figs. 2 and 4 but replaced one basin from the observational dataset with the $\mathrm{TEMP_{AC}}$ changes from each simulation for that basin. For example, in the "Atlantic" sensitivity test with the EN4 dataset, we replaced the EN4 Atlantic field with simulated $\mathrm{TEMP_{AC}}$ fields from each of the 51 HIST realizations, while preserving the original EN4 $\mathrm{TEMP_{AC}}$ changes in the Pacific and Indian Ocean Basins. This approach provides 51 "hybrid" $\mathrm{TEMP_{AC}}$ fields, each containing a different simulated Atlantic $\mathrm{TEMP_{AC}}$ field and the original Pacific and Indian fields from EN4. We use each of these 51 hybrid fields in our S/N analysis; a similar procedure is employed for the sensitivity test involving $\mathrm{TEMP_{AC}}$ changes in the Pacific Ocean Basin. By comparing the results from the hybrid "replace one basin" approach with the original S/N results, we can identify the influence of each basin on the model-observed S/N differences in Fig. 4.

Compared to the baseline analysis in Fig. 4c, replacing the observed Atlantic $\mathrm{TEMP_{AC}}$ field with model results markedly increases the S/N ratios estimated with IAP, Ishii, and EN4 (Fig. 9a). For the longest analysis periods, the ensemble average of the hybrid S/N results is now closer to the CMIP6 ensemble-mean S/N, particularly in the case of IAP. EN4—which was an outlier in the baseline S/N analysis in Fig. 4c—is now within the range of the original model S/N results. In contrast, replacing the observed $\mathrm{TEMP_{AC}}$ changes in the Pacific with model simulation output yields smaller S/N increases relative to the baseline results, and observed S/N behavior remains systematically lower than in CMIP6 (cf. Figs. 4c and 9b). These results indicate that the observed Atlantic $\mathrm{TEMP_{AC}}$ changes are probably the dominant contributory factor to the overall model-observed S/N differences in our baseline analysis (Fig. 4c). This result is consistent with the pattern differences between Figs. 1b,e,h and 2b: the observed trends are positive in the midlatitudes and in the interior layer of the North Atlantic, whereas the simulated fingerprint pattern shows a broad weakening of $\mathrm{TEMP_{AC}}$. Replacing the observed North Atlantic field (not shown) gives rise to results similar to those in Fig. 9a. While the South Atlantic also shows a significant model-observation difference in the zonal-mean pattern of $\mathrm{TEMP_{AC}}$ changes (cf. Figs. 1 and 2), the contribution from the South Atlantic to the overall S/N ratios is relatively small (see, e.g., the $\mathrm{TT_{AC}}$ results in Santer et al. 2018, 2022). This interhemispheric asymmetry in the forced response of $\mathrm{TEMP_{AC}}$ (Fig. 2) helps to explain why $\mathrm{TEMP_{AC}}$ changes in the North Atlantic have a large impact on the global S/N results.

8. Conclusions

The climate system is experiencing unprecedented changes due to anthropogenic activities (Eyring et al. 2021; Santer et al. 2023). Modification of the annual cycle of key climate variables is a key component of such changes. This study has systematically investigated changes in the annual cycle of temperature ($\mathrm{TEMP_{AC}}$) in the upper 300 m of the ocean. To study the causes of these changes, we employ a standard pattern-based detection and attribution (D&A) approach that relies on observational datasets and the latest CMIP6 model simulations of forced and unforced climate change. We examine the latitude–depth basin structure and causes of $\mathrm{TEMP_{AC}}$ changes, which have received relatively little attention to date.

Our D&A analysis confirms the existence of human influence on $\mathrm{TEMP_{AC}}$. The large-scale latitude–depth basin structure of $\mathrm{TEMP_{AC}}$ changes over 1980–2022 is broadly consistent across CMIP6 models and observations, with a robust increase in the annual cycle amplitudes at the surface and a notable decrease within the subsurface ocean, particularly at certain depths and regions. In the surface layer (above 30 m), the amplification of the annual cycle is much stronger in the midlatitudes of the NH, which is linked to the shoaling of the mixed layer (Shi et al. 2024). There is a distinctive meridional dipole structure at SH midlatitudes. The near-surface $\mathrm{TEMP_{AC}}$ results are physically and internally consistent with results from previous studies of changes in the annual cycle of tropospheric temperature ($\mathrm{TT_{AC}}$; Santer et al. 2018) and $\mathrm{SST_{AC}}$

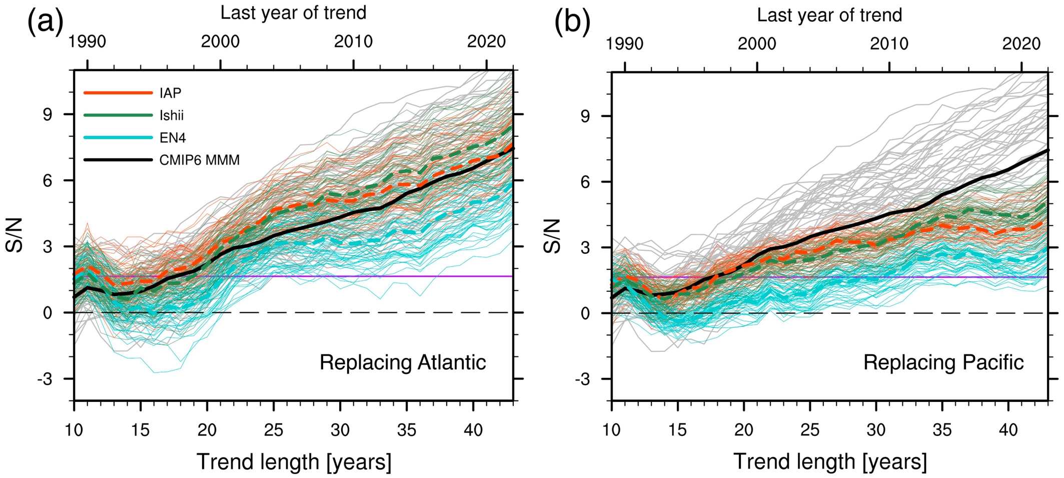

FIG. 9. S/N ratios for sensitivity tests involving replacement of observed $\mathrm{TEMP_{AC}}$ changes with model results. (a) Replacing each of the observed Atlantic $\mathrm{TEMP_{AC}}$ fields (i.e., IAP, Ishii, and EN4) with results from the HIST simulations. (b) As in (a), but with replacement of the observed Pacific $\mathrm{TEMP_{AC}}$ data with model results. The thicker dashed curves are the ensemble average of the "hybrid" results. The solid thick black curves and solid thin gray curves are identical to the original HIST S/N results in Fig. 4c and provide a reference for the magnitude of the S/N change arising from the sensitivity tests.

(Shi et al. 2024). A more novel aspect of our finding is that deep-reaching winter mixing transmits the surface warming signal to the bottom of the seasonal thermocline and warms winter temperatures, while in summer, the strengthening of the seasonal thermocline traps warming near the surface, thus increasing summer high temperatures at the surface. These changes result in increased $\mathrm{TEMP_{AC}}$ at the surface and decreased $\mathrm{TEMP_{AC}}$ in the deeper seasonal thermocline (between approximately 75–300 m).

We find that the fingerprint of externally forced $\mathrm{TEMP_{AC}}$ changes in CMIP6 simulations of historical climate change is identifiable with high statistical confidence in three different observational datasets and in 51 individual model realizations. Our analysis of single-forcing experiments indicates that human-caused changes in greenhouse gas emissions and anthropogenic aerosols are responsible for roughly 53% and 35% of the historical $\mathrm{TEMP_{AC}}$ changes (respectively). Sensitivity analyses reveal that our identification of human influence on $\mathrm{TEMP_{AC}}$ is robust to choices of analysis period either longer or shorter than our 1980–2022 baseline period.

There are, however, still discrepancies between S/N ratios obtained with modeled and observed $\mathrm{TEMP_{AC}}$ changes, particularly for changes over the 1980–2022 period of primary interest here. Observation-based S/N ratios are systematically lower than "model only" S/N ratios (see Fig. 4c). We find that this discrepancy arises primarily from differences between model and observed $\mathrm{TEMP_{AC}}$ changes in the Atlantic. Our study also highlights large discrepancies between the latitude–depth structure of $\mathrm{TEMP_{AC}}$ changes in the three observational datasets analyzed here, particularly between EN4 and the other two datasets (IAP and Ishii). Further investigation of the causes of this large structural uncertainty in observed ocean temperature data is urgently required.

Taken together with earlier work on tropospheric temperature (Santer et al. 2018, 2022) and SST (Shi et al. 2024), the changes in the vertical and latitudinal structure of $\mathrm{TEMP_{AC}}$ found here clearly show that anthropogenic impacts on the annual cycle are now detectable throughout the climate system, from the upper troposphere to the permanent ocean thermocline. These changes have a distinctive spatial and vertical structure and have the potential to influence both the productivity and distribution of marine species. For example, the habitat range of temperature-sensitive marine organisms is likely to be affected by the anthropogenically driven subsurface annual cycle changes identified here. Our findings of robust changes in the seasonality of ocean temperature may also have important implications for other biological and chemical properties of the ocean, such as ocean color and the uptake of oxygen and $\mathrm{CO_2}$ by the world's oceans. D&A methods provide a useful framework for examining whether such changes in marine biogeochemistry are consistent with the physical changes in ocean temperature reported here.

Acknowledgments. We acknowledge the World Climate Research Programme's Working Group on Coupled Modelling, which led the design of CMIP6 and coordinated the work, and we also thank individual climate modeling groups (listed in Table 1) for their efforts in performing all model simulations analyzed here. J.- R. S., Y.- O. K., and S. E. W. are supported by U.S. National Science Foundation under Grant OCE-2048336. B. D. S. and Y.- O. K. are supported by the Francis E. Fowler IV Center for Ocean and Climate at Woods Hole Oceanographic Institution (WHOI). We thank Lijing Cheng (IAP) for constructive comments on the manuscript.

Data availability statement. All datasets used in this study are publicly available. The CMIP6 historical and single-forcing simulation outputs are available on the Program for Climate Model Diagnostics and Intercomparison's Earth System Grid (https://esgf-node.llnl.gov/search/cmip6/). IAP data are available at https://climatedataguide.ucar.edu/climate-data/ocean-temperature-analysis-and-heat-content-estimate-institute-atmospheric-physics. The Ishii data are available at https://climate.mri-jma.go.jp/pub/ocean/ts/v7.3.1/temp/. EN4 data are available at https://metoffice.gov.uk/hadobs/en4/.

REFERENCES

Alexander, M. A., J. D. Scott, K. D. Friedland, K. E. Mills, J. A. Nye, A. J. Pershing, and A. C. Thomas, 2018: Projected sea surface temperatures over the 21st century: Changes in the mean, variability and extremes for large marine ecosystem regions of northern oceans. *Elementa*, **6**, 9, https://doi.org/10.1525/elementa.191.

Barnett, T. P., D. W. Pierce, K. M. AchutaRao, P. J. Gleckler, B. D. Santer, J. M. Gregory, and W. M. Washington, 2005: Penetration of human-induced warming into the world's oceans. *Science*, **309**, 284–287, https://doi.org/10.1126/science.1112418.

Bindoff, N. L., and Coauthors, 2013: Detection and attribution of climate change: From global to regional. *Climate Change 2013: The Physical Science Basis*, T. F. Stocker et al., Eds., Cambridge University Press, 867–952.

Blackport, R., J. C. Fyfe, and B. D. Santer, 2023: Robust human influence across the troposphere, surface, and ocean: A multivariate analysis. *J. Climate*, **36**, 7879–7891, https://doi.org/10.1175/JCLI-D-23-0068.1.

Bonfils, C. J. W., B. D. Santer, J. C. Fyfe, K. Marvel, T. J. Phillips, and S. R. H. Zimmerman, 2020: Human influence on joint changes in temperature, rainfall and continental aridity. *Nat. Climate Change*, **10**, 726–731, https://doi.org/10.1038/s41558-020-0821-1.

Chemke, R., and J. Yuval, 2023: Human-induced weakening of the Northern Hemisphere tropical circulation. *Nature*, **617**, 529–532, https://doi.org/10.1038/s41586-023-05903-1.

Chen, C., and G. Wang, 2015: Role of North Pacific mixed layer in the response of SST annual cycle to global warming. *J. Climate*, **28**, 9451–9458, https://doi.org/10.1175/JCLI-D-14-00349.1.

Cheng, L., G. Wang, J. P. Abraham, and G. Huang, 2018: Decadal ocean heat redistribution since the late 1990s and its association with key climate modes. *Climate*, **6**, 91, https://doi.org/10.3390/cli6040091.

——, J. Abraham, Z. Hausfather, and K. E. Trenberth, 2019: How fast are the oceans warming? *Science*, **363**, 128–129, https://doi.org/10.1126/science.aav7619.

Deser, C., A. S. Phillips, M. A. Alexander, and B. V. Smoliak, 2014: Projecting North American climate over the next 50 years: Uncertainty due to internal variability. *J. Climate*, **27**, 2271–2296, https://doi.org/10.1175/JCLI-D-13-00451.1.

——, and Coauthors, 2020: Isolating the evolving contributions of anthropogenic aerosols and greenhouse gases: A new CESM1 large ensemble community resource. *J. Climate*, **33**, 7835–7858, https://doi.org/10.1175/JCLI-D-20-0123.1.

Duan, J., and Coauthors, 2019: Detection of human influences on temperature seasonality from the nineteenth century. *Nat. Sustainability*, **2**, 484–490, https://doi.org/10.1038/s41893-019-0276-4.

Dwyer, J. G., M. Biasutti, and A. H. Sobel, 2012: Projected changes in the seasonal cycle of surface temperature. *J. Climate*, **25**, 6359–6374, https://doi.org/10.1175/JCLI-D-11-00741.1.

Eyring, V., S. Bony, G. A. Meehl, C. A. Senior, B. Stevens, R. J. Stouffer, and K. E. Taylor, 2016: Overview of the Coupled Model Intercomparison Project Phase 6 (CMIP6) experimental design and organization. *Geosci. Model Dev.*, **9**, 1937–1958, https://doi.org/10.5194/gmd-9-1937-2016.

——, and Coauthors, 2021: Human influence on the climate system. *Climate Change 2021: The Physical Science Basis*, V. Masson-Delmotte et al., Eds., Cambridge University Press, 423–552.

Gillett, N. P., J. C. Fyfe, and D. E. Parker, 2013: Attribution of observed sea level pressure trends to greenhouse gas, aerosol, and ozone changes. *Geophys. Res. Lett.*, **40**, 2302–2306, https://doi.org/10.1002/grl.50500.

——, and Coauthors, 2016: The Detection and Attribution Model Intercomparison Project (DAMIP v1.0) contribution to CMIP6. *Geosci. Model Dev.*, **9**, 3685–3697, https://doi.org/10.5194/gmd-9-3685-2016.

Gleckler, P. J., and Coauthors, 2012: Human-induced global ocean warming on multidecadal timescales. *Nat. Climate Change*, **2**, 524–529, https://doi.org/10.1038/nclimate1553.

——, P. J. Durack, R. J. Stouffer, G. C. Johnson, and C. E. Forest, 2016: Industrial-era global ocean heat uptake doubles in recent decades. *Nat. Climate Change*, **6**, 394–398, https://doi.org/10.1038/nclimate2915.

Good, S. A., M. J. Martin, and N. A. Rayner, 2013: EN4: Quality controlled ocean temperature and salinity profiles and monthly objective analyses with uncertainty estimates. *J. Geophys. Res. Oceans*, **118**, 6704–6716, https://doi.org/10.1002/2013JC009067.

Gouretski, V., and F. Reseghetti, 2010: On depth and temperature biases in bathythermograph data: Development of a new correction scheme based on analysis of a global ocean database. *Deep-Sea Res. I*, **57**, 812–833, https://doi.org/10.1016/j.dsr.2010.03.011.

Hasselmann, K., 1979: On the signal-to-noise problem in atmospheric response studies. *Meteorology of Tropical Oceans*, D. B. Shawn, Ed., Royal Meteorological Society, 251–259.

Hawkins, E., and R. Sutton, 2009: The potential to narrow uncertainty in regional climate predictions. *Bull. Amer. Meteor. Soc.*, **90**, 1095–1108, https://doi.org/10.1175/2009BAMS2607.1.

Hegerl, G. C., H. von Storch, K. Hasselmann, B. D. Santer, U. Cubasch, and P. D. Jones, 1996: Detecting greenhouse-gas-induced climate change with an optimal fingerprint method. *J. Climate*, **9**, 2281–2306, https://doi.org/10.1175/1520-0442(1996)009<2281:DGGICC>2.0.CO;2.

Ishii, M., A. Shouji, S. Sugimoto, and T. Matsumoto, 2005: Objective analyses of sea-surface temperature and marine meteorological variables for the 20th century using ICOADS and the Kobe Collection. *Int. J. Climatol.*, **25**, 865–879, https://doi.org/10.1002/joc.1169.

Jo, A. R., J.-Y. Lee, A. Timmermann, F.-F. Jin, R. Yamaguchi, and A. Gallego, 2022: Future amplification of sea surface temperature seasonality due to enhanced ocean stratification. *Geophys. Res. Lett.*, **49**, e2022GL098607, https://doi.org/10.1029/2022GL098607.

Lehner, F., C. Deser, N. Maher, J. Marotzke, E. Fischer, L. Brunner, R. Knutti, and E. Hawkins, 2020: Partitioning climate projection uncertainty with multiple large ensembles and CMIP5/6. *Earth System Dyn.*, **11**, 491–508, https://doi.org/10.5194/esd-2019-93.

Levitus, S., J. Antonov, and T. Boyer, 2005: Warming of the world ocean, 1955–2003. *Geophys. Res. Lett.*, **32**, L02604, https://doi.org/10.1029/2004GL021592.

Liu, F., J. Lu, Y. Luo, Y. Huang, and F. Song, 2020: On the oceanic origin for the enhanced seasonal cycle of SST in the midlatitudes under global warming. *J. Climate*, **33**, 8401–8413, https://doi.org/10.1175/JCLI-D-20-0114.1.

——, F. Song, and Y. Luo, 2024: Human-induced intensified seasonal cycle of sea surface temperature. *Nat. Commun.*, **15**, 3948, https://doi.org/10.1038/s41467-024-48381-3.

Lyman, J. M., and G. C. Johnson, 2008: Estimating annual global upper-ocean heat content anomalies despite irregular in situ ocean sampling. *J. Climate*, **21**, 5629–5641, https://doi.org/10.1175/2008JCLI2259.1.

Marshall, G. J., 2003: Trends in the southern annular mode from observations and reanalyses. *J. Climate*, **16**, 4134–4143, https://doi.org/10.1175/1520-0442(2003)016<4134:TITSAM>2.0.CO;2.

Marvel, K., and C. Bonfils, 2013: Identifying external influences on global precipitation. *Proc. Natl. Acad. Sci. USA*, **110**, 19 301–19 306, https://doi.org/10.1073/pnas.1314382110.

——, M. Biasutti, C. Bonfils, K. E. Taylor, Y. Kushnir, and B. I. Cook, 2017: Observed and projected changes to the precipitation annual cycle. *J. Climate*, **30**, 4983–4995, https://doi.org/10.1175/JCLI-D-16-0572.1.

Meyssignac, B., and Coauthors, 2019: Measuring global Ocean Heat Content to estimate the Earth energy imbalance. *Front. Mar. Sci.*, **6**, 432, https://doi.org/10.3389/fmars.2019.00432.

Min, S.-K., X. Zhang, F. W. Zwiers, and T. Agnew, 2008: Human influence on Arctic sea ice detectable from early 1990s onwards. *Geophys. Res. Lett.*, **35**, L21701, https://doi.org/10.1029/2008GL035725.

Pierce, D. W., T. P. Barnett, K. M. AchutaRao, P. J. Gleckler, J. M. Gregory, and W. M. Washington, 2006: Anthropogenic warming of the oceans: Observations and model results. *J. Climate*, **19**, 1873–1900, https://doi.org/10.1175/JCLI3723.1.

——, P. J. Gleckler, T. P. Barnett, B. D. Santer, and P. J. Durack, 2012: The fingerprint of human-induced changes in the ocean's salinity and temperature fields. *Geophys. Res. Lett.*, **39**, L21704, https://doi.org/10.1029/2012GL053389.

Po-Chedley, S., B. D. Santer, S. Fueglistaler, M. D. Zelinka, P. J. Cameron-Smith, J. F. Painter, and Q. Fu, 2021: Natural variability contributes to model–satellite differences in tropical tropospheric warming. *Proc. Natl. Acad. Sci. USA*, **118**, e2020962118, https://doi.org/10.1073/pnas.2020962118.

——, J. T. Fasullo, N. Siler, Z. M. Labe, E. A. Barnes, C. J. W. Bonfils, and B. D. Santer, 2022: Internal variability and forcing influence model–satellite differences in the rate of tropical tropospheric warming. *Proc. Natl. Acad. Sci. USA*, **119**, e2209431119, https://doi.org/10.1073/pnas.2209431119.

Qian, C., and X. Zhang, 2015: Human influences on changes in the temperature seasonality in mid- to high-latitude land areas. *J. Climate*, **28**, 5908–5921, https://doi.org/10.1175/JCLI-D-14-00821.1.

Roemmich, D., J. Gilson, R. Davis, P. Sutton, S. Wijffels, and S. Riser, 2007: Decadal spinup of the South Pacific subtropical gyre. *J. Phys. Oceanogr.*, **37**, 162–173, https://doi.org/10.1175/JPO3004.1.

Santer, B. D., and Coauthors, 1996: A search for human influences on the thermal structure of the atmosphere. *Nature*, **382**, 39–46, https://doi.org/10.1038/382039a0.

——, and Coauthors, 2007: Identification of human-induced changes in atmospheric moisture content. *Proc. Natl. Acad. Sci. USA*, **104**, 15 248–15 253, https://doi.org/10.1073/pnas.0702872104.

——, and Coauthors, 2013: Identifying human influences on atmospheric temperature. *Proc. Natl. Acad. Sci. USA*, **110**, 26–33, https://doi.org/10.1073/pnas.1210514109.

——, and Coauthors, 2018: Human influence on the seasonal cycle of tropospheric temperature. *Science*, **361**, eaas8806, https://doi.org/10.1126/science.aas8806.

——, J. C. Fyfe, S. Solomon, J. F. Painter, C. Bonfils, G. Pallotta, and M. D. Zelinka, 2019: Quantifying stochastic uncertainty in detection time of human-caused climate signals. *Proc. Natl. Acad. Sci. USA*, **116**, 19 821–19 827, https://doi.org/10.1073/pnas.1904586116.

——, and Coauthors, 2022: Robust anthropogenic signal identified in the seasonal cycle of tropospheric temperature. *J. Climate*, **35**, 6075–6100, https://doi.org/10.1175/JCLI-D-21-0766.1.

——, and Coauthors, 2023: Exceptional stratospheric contribution to human fingerprints on atmospheric temperature. *Proc. Natl. Acad. Sci. USA*, **120**, e2300758120, https://doi.org/10.1073/pnas.2300758120.

Shi, J.-R., S.-P. Xie, and L. D. Talley, 2018: Evolving relative importance of the Southern Ocean and North Atlantic in anthropogenic ocean heat uptake. *J. Climate*, **31**, 7459–7479, https://doi.org/10.1175/JCLI-D-18-0170.1.

——, L. D. Talley, S.-P. Xie, Q. Peng, and W. Liu, 2021: Ocean warming and accelerating Southern Ocean zonal flow. *Nat. Climate Change*, **11**, 1090–1097, https://doi.org/10.1038/s41558-021-01212-5.

——, Y.-O. Kwon, and S. E. Wijffels, 2022: Two distinct modes of climate responses to the anthropogenic aerosol forcing changes. *J. Climate*, **35**, 3445–3457, https://doi.org/10.1175/JCLI-D-21-0656.1.

——, ——, and ——, 2023: Subsurface ocean temperature responses to the anthropogenic aerosol forcing in the North Pacific. *Geophys. Res. Lett.*, **50**, e2022GL101035, https://doi.org/10.1029/2022GL101035.

——, B. D. Santer, Y.-O. Kwon, and S. E. Wijffels, 2024: The emerging human influence on the seasonal cycle of sea surface temperature. *Nat. Climate Change*, **14**, 364–372, https://doi.org/10.1038/s41558-024-01958-8.

Silvy, Y., E. Guilyardi, J.-B. Sallée, and P. J. Durack, 2020: Human-induced changes to the global ocean water masses and their time of emergence. *Nat. Climate Change*, **10**, 1030–1036, https://doi.org/10.1038/s41558-020-0878-x.

Stott, P. A., S. F. B. Tett, G. S. Jones, M. R. Allen, J. F. B. Mitchell, and G. J. Jenkins, 2000: External control of 20th century temperature by natural and anthropogenic forcings. *Science*, **290**, 2133–2137, https://doi.org/10.1126/science.290.5499.2133.

Swart, N. C., and J. C. Fyfe, 2012: Observed and simulated changes in the Southern Hemisphere surface westerly wind-stress. *Geophys. Res. Lett.*, **39**, L16711, https://doi.org/10.1029/2012GL052810.

——, S. T. Gille, J. C. Fyfe, and N. P. Gillett, 2018: Recent Southern Ocean warming and freshening driven by greenhouse gas emissions and ozone depletion. *Nat. Geosci.*, **11**, 836–841, https://doi.org/10.1038/s41561-018-0226-1.

Terray, L., L. Corre, S. Cravatte, T. Delcroix, G. Reverdin, and A. Ribes, 2012: Near-surface salinity as nature's rain gauge to detect human influence on the tropical water cycle. *J. Climate*, **25**, 958–977, https://doi.org/10.1175/JCLI-D-10-05025.1.

Thompson, D. W. J., and S. Solomon, 2002: Interpretation of recent Southern Hemisphere climate change. *Science*, **296**, 895–899, https://doi.org/10.1126/science.1069270.

van den Dool, H. M., S. Saha, and Å. Johansson, 2000: Empirical orthogonal teleconnections. *J. Climate*, **13**, 1421–1435, https://doi.org/10.1175/1520-0442(2000)013<1421:EOT>2.0.CO;2.

von Schuckmann, K., and Coauthors, 2020: Heat stored in the Earth system: Where does the energy go? *Earth Syst. Sci. Data*, **12**, 2013–2041, https://doi.org/10.5194/essd-12-2013-2020.

Wijffels, S., D. Roemmich, D. Monselesan, J. Church, and J. Gilson, 2016: Ocean temperatures chronicle the ongoing warming of Earth. *Nat. Climate Change*, **6**, 116–118, https://doi.org/10.1038/nclimate2924.

Zhang, X., F. W. Zwiers, G. C. Hegerl, F. H. Lambert, N. P. Gillett, S. Solomon, P. A. Stott, and T. Nozawa, 2007: Detection of human influence on twentieth-century precipitation trends. *Nature*, **448**, 461–465, https://doi.org/10.1038/nature06025.

Zhang, Y., C. Chen, S. Hu, G. Wang, K. McMonigal, and S. M. Larson, 2024: Summer westerly wind intensification weakens Southern Ocean seasonal cycle under global warming. *Geophys. Res. Lett.*, **51**, e2024GL109715, https://doi.org/10.1029/2024GL109715.